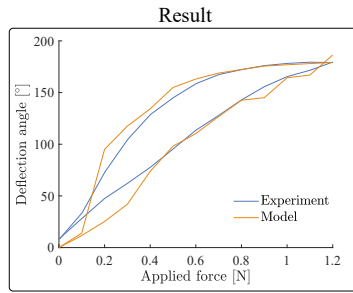
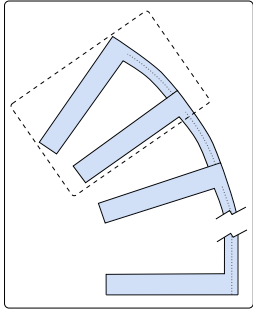


Graphical Abstract

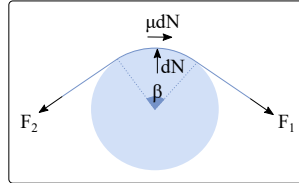
A Large Displacement Model for Superelastic Material Side-Notched Tube Instruments

Julie Legrand, Mouloud Ourak, Tom Vandebroek, Emmanuel Vander Poorten

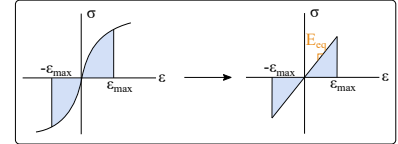
Successive deformation calculation



Friction: Capstan equation



Non-linearity: ϵ -dependant E_{eq}



Highlights

A Large Displacement Model for Superelastic Material Side-Notched Tube Instruments

Julie Legrand, Mouloud Ourak, Tom Vandebroek, Emmanuel Vander Poorten

- Superelasticity of a material modelled using an equivalent, strain dependent, linear elastic modulus.
- Non-constant curvature deformation modeled by calculating the deformation of each separate section successively.
- Static friction plays an important role in superelastic material side-notched tube instruments.
- Static model solution for the loading and unloading cases.
- Heat-treatment of the NiTi to reduce the NiTi stress plateau and decrease the required load.

A Large Displacement Model for Superelastic Material Side-Notched Tube Instruments

Julie Legrand^{a,*}, Mouloud Ourak^a, Tom Vandebroek^a and Emmanuel Vander Poorten^a

^aRobotics, Automation and Mechatronics group (RAM), Katholieke Universiteit Leuven, Heverlee B-3001, Belgium

ARTICLE INFO

Keywords:

statics
analytical model
superelastic material
nitinol
friction modeling
flexible robotic

ABSTRACT

Side-notched tube structures made of superelastic material are increasingly being studied in surgical robotics as they can easily be integrated into surgical instruments and offer the surgeon enhanced dexterity. Their simple design and ability to achieve large bending angles and small bending radii make them particularly suited for use in constrained workspace surgery. Up to now, however, no model has been able to accurately predict the behavior of such types of structures for large bending angles. This study, therefore, proposes a novel approach to model large displacements of side-notched tubes taking into account the superelasticity of the material, the non-constant curvature of the side-notched structure, as well as the friction induced by the actuating wire. More specifically, an equivalent, strain dependent, linear elastic modulus is used to model the superelastic behavior of the instrument's material. The deformation of each separate section of the side-notched tube is calculated successively to capture the non-constant curvature of the NiTi backbone. The capstan equation is used to model cable friction. The model was tested on four samples of 2.3mm diameter and was able to predict the bending angle of the side-notched tubes with a root mean square error (RMSE) of as low as 5.4° (3.1%) and the position of each notch with an RMSE of as low as 0.33mm (2.5%) across its entire bending range (0° to 180°). The model was demonstrated for both tension and relaxation of the actuating wire.

1. Introduction

A notched tube structure or backbone consists of a tube into which notches have been cut in order to reduce its stiffness and allow the structure to bend when it is externally actuated by a wire. Figure 1 provides an example of such structures. Notched tubes are usually made out of a (super)elastic material like Nitinol (NiTi) or PolyEther Ether Ketone (PEEK) [1, 2, 3]. Notched tube backbones can be easily manufactured and miniaturized thanks to their simple shape. They can also withstand large bending angles and small bending radii, and are able to return to their rest configuration. However, the friction existing between the wire and the (super)elastic structure is known to affect its controllability [4]. For superelastic NiTi backbones, a hysteretic effect is also present when loading and unloading the structure. This complicates the control, the reachable bandwidth, and the precision. Compared to steel, NiTi can take larger strains and is biocompatible, which makes it particularly suited for use in constrained workspace surgery in which high flexibility is desired [5]. NiTi notched tubes have been proposed for various surgical applications such as laparoscopy [6, 7], neuroendoscopy [8, 9, 10], treatment of osteolytic lesions [11, 12] and inspection of the middle ear [13]. Table 1 provides an extensive overview of such works. For each concept, the shape of the notches (pattern), the Degrees of Freedom (DoFs) unidirectional (*ud*) or bidirectional (*bd*), the outer diameter (OD), the wall thickness (WT) and the length (L) of the flexible structure are presented. The maximum bending angle (BA), the minimum bending radius (BR) and



Figure 1: Side-notched NiTi backbone undergoing an increasing actuation force from the pull wire. The backbone shows a non-constant curvature as it bends: the first notch is deformed before the last one.

the characteristic strain (CS), which is defined as the ratio between the outer diameter and the minimum bending radius, are also indicated. Figure 2 visualises these last three geometric parameters. The characteristic strain corresponds to the maximum strain undergone by the structure's outer fiber. The reported load that has to be applied to the wire to reach the maximum bending angle is listed in the next to last column. Finally, the main physical law that was used to model the static behavior of each backbone is mentioned in the last column.

What is noteworthy in Table 1 is that the pattern used by York *et al.* [15] and Eastwood *et al.* [8], i.e. a side-notched pattern, can reach large bending angles while keeping the bending radius small, especially in comparison to the other reported patterns. This type of side-notched backbone is therefore worth investigating as it might also be of use for the design of surgical instruments with large bending angles (reaching up to 180°) and small bending radii (typically below 3mm). The fact that this simple pattern only allows for one unidirectional bending DoF is not necessarily a prob-

*This work was supported by a grant from the Belgian FWO [SB/1S98418N] and PRESlice (C22/16/015), an internal KU Leuven grant.

*Corresponding author: julie.legrand@kuleuven.be
ORCID(s):

Table 1
Extensive state of the art of NiTi notched backbone designs and their corresponding static models

Author	Pattern	DoF	(OD, WT, L) [mm]	(BA [°], BR [mm], CS)	Max. load [N]	Quasi-static model
Fisher (1999) [6]		1_{ud}	(10.5, 0.17, 60)	(90, 17.5*, 0.6*)	4.4	-
Peirs (2002) [14]		2	(4.7, 0.4, 37)	(96, 25*, 0.19*)	8	-
Kutzer (2011) [11]		1_{bd}	(5.99, 1, 40*)	(135, 20.4*, 0.29*)	44	-
Wei (2012) [7]		1_{bd}	(8, 0.5, 20*)	(17, -, -)	15	Timoshenko's beam theory
Murphy (2014) [12]		1_{bd}	(6, 1, 35)	(90, -, -)	22.2	Energy minimization
York (2015) [15]		1_{ud}	(1.16, 0.15, 5.61)	(90, 3.1*, 0.37*)	5	Castigliano's 1st theorem
Eastwood (2016) [8]		1_{ud}	(1.8, 0.2, 7.66)	(90, 3.5*, 0.51*)	20	Castigliano's 2nd theorem
Eastwood (2017) [9]		1_{ud}	(1.24, 0.1, 80*)	(80, 4.5*, 0.28*)	1.5	Castigliano's 1st theorem
Fichera (2017) [13]		1_{ud}	(1.8, 0.1, 155)	(180, -, -)	-	Castigliano's 1st theorem
Francis (2017) [16]		2	(1.37, 0.22, -)	(70, 10, 0.14)	10	-
Chitalia (2020) [10]	1_{bd}	(1.93, 0.22, 5.5)	(60, 3.5*, 0.55*)	6.5	Castigliano's 1st theorem	

*Values deduced from provided instrument pictures.

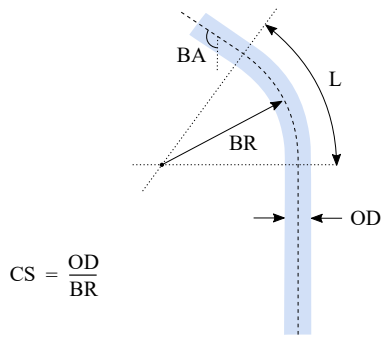


Figure 2: Bending angle (BA), bending radius (BR), characteristic strain (CS), outer diameter (OD) and bendable length (L) of non-protrusible continuous (super)elastic structures.

lem in many surgical procedures. In fact, complex endoscopic instruments with multiple degrees of freedom have been shown to impede the surgeon's task performance [17]. By limiting the configuration space, the surgeon's mental workload can be reduced so that they can focus on more critical aspects of the procedure itself [17]. However, it is important to note that the characteristic strain (CS) of such a side-notched pattern is larger than for other types of patterns (see Fisher, York and Eastwood (2016) in Table 1). This means that the strain on the structure's outer fiber (the maximum strain) is expected to be high, and the backbone will undergo large displacements.

Table 1 shows that, so far, the models used for the quasi-static modeling of the notched NiTi backbones are either

based on beam theory, which considers the whole backbone as a beam to which the first or second Castigliano's theorem is applied [7, 15, 8, 9, 13], or solved as a constrained energy minimization problem [12]. These models have shown adequate controllability for low bending angles (i.e. from 0° to 90°). Fichera *et al.* reported a model capable of accurately predicting the instrument's bending angle up to 160°, but the instrument is long and contains a large number of small notches. The bending radius is therefore expected to be large and the deformation of each notch to be small [13]. All models listed in Table 1 make strong assumptions that do not hold for the large displacements that occur when driving side-notched instruments over large bending angles and small bending radii. Moreover, NiTi is a superelastic material with a highly nonlinear stress-strain curve and, as such, it differs significantly from materials with mainly linear behavior such as steel (Fig. 3). Hence, the linear material hypotheses made by Wei *et al.* [7] and Eastwood *et al.* [8] cannot be applied when researching NiTi large displacements. Also, the constant curvature bending assumption made by York *et al.* [15], Eastwood *et al.* [9] and Fichera *et al.* [13] is not valid either. Indeed, it was experimentally observed during this study that, for approximately equal sized side-notches, the first distal notch of the NiTi backbone bends substantially before the last one starts bending. (Fig. 1). This phenomenon is caused by manufacturing inaccuracies and friction.

In order to overcome the limitations of the previous approaches, this paper proposes a static model for large displacements of side-notched tube instruments. This model takes the mate-

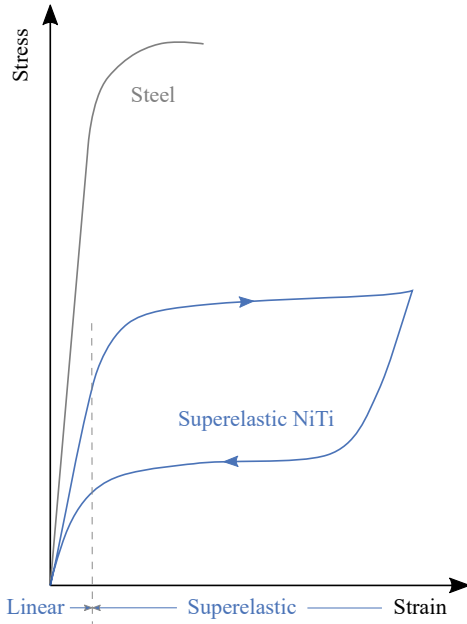


Figure 3: Stress-strain curve of steel (grey) and superelastic NiTi (blue). NiTi shows a linear behavior at small strains and a superelastic behavior at higher strains as well as hysteresis.

material's superelasticity into account as well as the backbone's non-constant curvature bending. Additionally, it takes into consideration the friction that is present between the pull wire and the backbone. This kind of static model which uses only a limited number of hypotheses has, to the best of the authors' knowledge, never been reported before. The presented model only requires the geometrical dimensions of the side-notched backbone, its material properties and an estimate of the friction coefficient between the wire and the backbone as input. It provides an accurate estimate of the shape of the instrument under loading and unloading from the pull wire. The model can be used to design side-notched tube portions or wrists for limited workspace surgical procedures as well as to improve the precision of controllers.

The paper is structured as follows: in Section 2, the static model for large displacements of side-notched tube instruments is described. The model is then validated by comparing its output to experiments in Section 3. More specifically, four different notched backbone geometries are tested under loading from the pull wire. The unloading case is also assessed for one of the samples. In Section 4, the factors influencing the accuracy of the static model are discussed and possible applications of the model are proposed. Finally, in Section 5, conclusions regarding the present study are made and some directions for future research are provided.

2. Static model

The side-notched NiTi backbone is manufactured by cutting notches with a depth g_j from a tube of external radius R_o and internal radius R_i . This particular structure can be seen as a concatenation of j rigid *teeth* portions (part 1 in

Fig. 4b) of height h_{t_j} , and j flexible *beam* portions (part 2 in Fig. 4b) of height L_j ($j \in [1, n]$, with n , the total number of notches). The *beam* and *tooth* portion situated most distally correspond to $j = 1$. A wire is attached to the extremity of the backbone, on the first *tooth* (Fig. 4). The structure can thus be deflected by increasing or releasing the tension in the wire.

Even though the proposed approach is more general than in prior studies, some general hypotheses are still adopted to keep the model's complexity manageable. In the following model, it is assumed that:

1. the superelastic stress-strain curve of the material can be approximated by an equivalent, strain dependent, linear elastic modulus;
2. the deformation of the backbone's *teeth* (part 1 in Fig. 4) can be ignored due to the specific aspect ratio;
3. the deformations are strictly planar;
4. the effect of the shear stress on the deformation can be neglected;
5. the buckling caused by the axial load on the *beam* portions can be neglected;
6. the normal forces exerted by the cable on the backbone have a negligible effect on the bending of the beam sections;
7. the friction present between the tension wire and the backbone can be modeled using the Capstan equation.

The validity of each of these seven hypotheses is further discussed in Appendix A.

The structure of this section is as follows. First, the superelasticity of the material, as well as the deformation of the

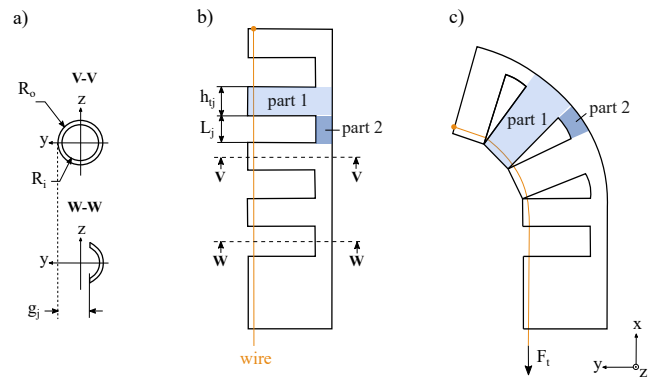


Figure 4: Actuation of a side-notched NiTi backbone via a tension wire with a tension force F_t ; part 1 indicates a rigid *tooth*; part 2 indicates a flexible *beam*; a) cross-sectional view; b) rest position; c) deflected configuration.

flexible beams of which the backbone consists will be tackled in subsection 2.1. Subsequently, one complete section of the notched backbone (i.e. composed of one rigid *tooth* and one flexible *beam*) will be analyzed in 2.3. This will then be followed in 2.3 by the presentation of the static equations of the entire notched backbone. Finally, in subsection 2.4, a method based on the Capstan equation is introduced to model cable friction.

2.1. Large displacement of the superelastic flexible beams of the notched backbone.

Each flexible beam portion j (with $j \in [1, n]$) of the NiTi backbone can be seen as a cantilever beam of length L_j with an annular segment section. In the case of the top section ($j = 1$), the pull wire applies a load F_{app1} at the tooth extremity as well as a normal force N_1 and friction f_1 (Fig. 5). Those applied forces on the first tooth extremity can be represented by a bending moment M_1 that is applied to the top of the beam portion (Fig. 5). As hypothesis 5 states, it is assumed that the axial forces will not cause deformation of the beam portion. Moreover, the normal forces N_j applied by the cable are significantly smaller than F_{app1} . Therefore, it is assumed that the bending of the beam portions caused by these normal forces is insignificant in comparison to the bending caused by M_j (hypothesis 6). For the lower sections, as explained further in the text, the bending moment M_j applied to the j^{th} beam portion extremity follows from the moments upon the upper sections as well as the cable normal force and friction applied to the j^{th} tooth.

2.1.1. Material superelasticity

Large displacements of the beam portion are expected since the aim is to create large bending angles across the whole backbone while keeping the bending radius small. It is therefore expected that the material will reach strains that are situated in the superelastic part of the NiTi stress-strain curve (Fig. 3).

In order to model this superelastic behavior, an equivalent, strain dependent, linear elastic modulus is proposed. To find this equivalent elastic modulus, the equation of the inner bending moment can first be expressed according to the normal stress σ :

$$M = \int_{A_T} \sigma y dA = \iint_{A_T} \sigma y dy dz, \quad (1)$$

where y is the coordinate normal to the neutral axis and dA is an infinitesimal area on the flexible beam cross-section A_T . Then, the standard strain-curvature expression for an infinitesimal element dy can be used, i.e.,

$$dy = \rho(s) d\epsilon, \quad (2)$$

with the radius of curvature $\rho(s) \geq 0$ for all s (where $0 \leq s \leq L$). By using (2) in (1), the following equation can be

obtained:

$$M = \rho(s)^2 \int_{z_{min}}^{z_{max}} \int_{\epsilon_{min}}^{\epsilon_{max}} \sigma \epsilon d\epsilon dz, \quad (3)$$

with z_{min} and z_{max} representing the area bounds in the z direction, and ϵ_{max} and ϵ_{min} representing the maximum and minimum strain undergone by the beam, respectively, i.e. the strain at its outer fiber. The parameter s represents the curvilinear coordinate along the neutral axis measured from the proximal base of the instrument (Fig. 5).

Under the assumption that the compression and tension of the material show symmetry in the σ - ϵ plane, one can derive that $\epsilon_{min} = -\epsilon_{max}$ (see Fig. 6). By using this extra hypothesis, (3) can be written as:

$$M = 2\rho(s)^2 \int_{z_{min}}^{z_{max}} \int_0^{\epsilon_{max}} \sigma \epsilon d\epsilon dz, \quad (4)$$

Eq. (4) is a general equation holding for any kind of material of known stress function $\sigma(\epsilon)$ showing symmetry in the σ - ϵ plane. In the case of a linear material of Young modulus E , (4) takes the following form:

$$M = 2\rho(s)^2 \int_{z_{min}}^{z_{max}} \frac{E \epsilon_{max}^3}{3} dz. \quad (5)$$

Equalizing the expressions of the bending moment for a superelastic material (Eq. 4) and for a linear material (Eq. 5) allows us to obtain the same radius of curvature ($\rho(s)$) for a linear material as for a superelastic material of stress function $\sigma(\epsilon)$. More specifically, this means that an equivalent, strain dependant Young modulus E can be defined that can

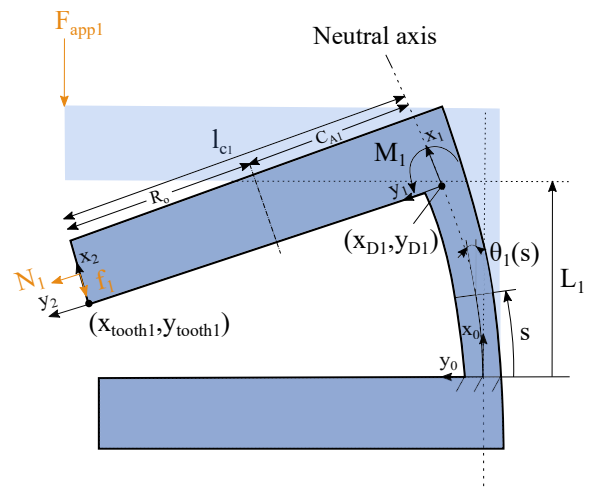


Figure 5: Deformed section of the upper notch ($j = 1$) of the side-notched backbone resulting from a force F_{app} applied to the tooth tip by the pull wire. The friction between the backbone and the pull wire is not taken into consideration in this figure.

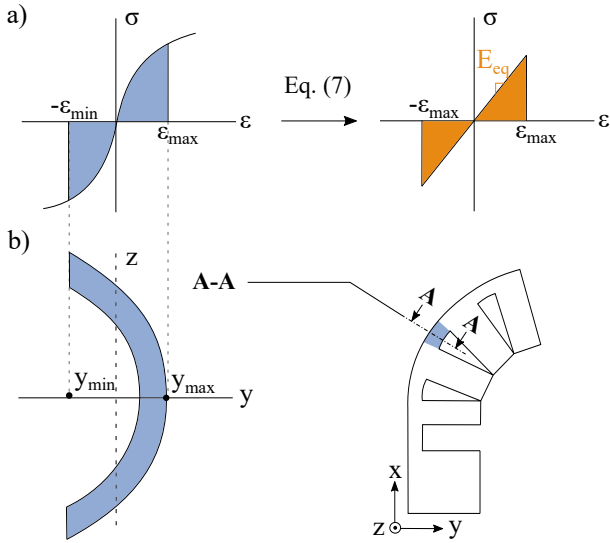


Figure 6: Graphic representation of the equivalent, strain dependent, linear elastic modulus E_{eq} ; a) stress-strain loading curve of the superelastic material (left) used to calculate the E_{eq} (right) based on a specific ϵ_{max} by means of (7); b) cross-section of a deformed flexible backbone beam.

represent the same beam's radius of curvature as a superelastic material of stress function $\sigma(\epsilon)$.

In (4) and (5), the integral in z is a constant and only depends on the beam geometry. Therefore, equalizing both Eqs. (4) and (5) gives:

$$\frac{E\epsilon_{max}^3}{3} = \int_0^{\epsilon_{max}} \sigma\epsilon d\epsilon. \quad (6)$$

Finally, by introducing the equivalent Young modulus E , now expressed as E_{eq} , it becomes possible to obtain a linear approximation of a specific bending for a superelastic material with a stress function $\sigma(\epsilon)$ (Fig. 6). E_{eq} can be expressed by rearranging (6):

$$E_{eq}(\epsilon_{max}) = \frac{3}{\epsilon_{max}^3} \int_0^{\epsilon_{max}} \sigma\epsilon d\epsilon. \quad (7)$$

The calculation of the integral in (7) can be obtained by using experimental data from the superelastic material.

Adopting this E_{eq} now allows us to use linear equations for large beam displacements. Therefore, Eq. (1) can first be rewritten as:

$$M = \iint_{A_T} E_{eq}(\epsilon_{max})\epsilon y dy dz. \quad (8)$$

Then, by inserting (2) in (8), the following equation can be obtained:

$$M = \frac{E_{eq}(\epsilon_{max})}{\rho(s)} \iint_{A_T} y^2 dy dz. \quad (9)$$

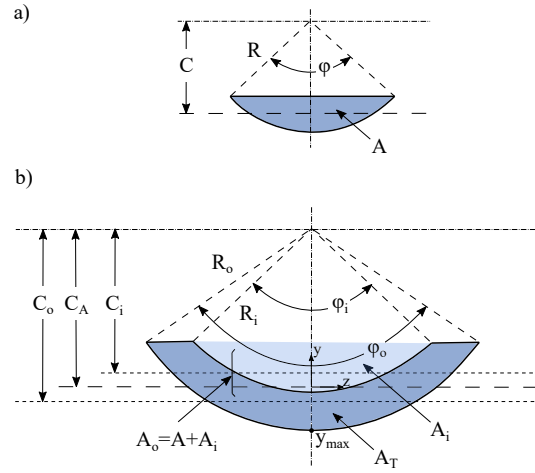


Figure 7: Geometrical scheme used to calculate the centroid of the NiTi backbone beam section; a) general case for a circular segment A ; b) cross section of the NiTi backbone flexible beam obtained by subtraction of the circular segments A_i from A_o .

Finally, (9) can be written in terms of the second moment of area of the flexible beam:

$$M = \frac{E_{eq}(\epsilon_{max})I_{CA}}{\rho(s)}, \quad (10)$$

where I_{CA} is the second moment of area of the flexible beam portion, which is calculated as described in Section 2.1.2.

2.1.2. Second moment of area of the flexible beam portion

The centroid C of a circular segment A , delimited by its spanning angles φ and radius R (Fig. 7a), can be expressed as:

$$C = \frac{4R\sin^3(\frac{\varphi}{2})}{3(\varphi - \sin\varphi)}. \quad (11)$$

As Roark *et al.* [18] describe, the moment of inertia of this circular segment A , with respect to its centroid C is given by:

$$I_C = \begin{cases} \frac{R^4}{4} \left(\frac{\varphi}{2} - \sin\frac{\varphi}{2}\cos\frac{\varphi}{2} + 2\sin^3\frac{\varphi}{2}\cos\frac{\varphi}{2} - \frac{16\sin^6\frac{\varphi}{2}}{9(\frac{\varphi}{2} - \sin\frac{\varphi}{2}\cos\frac{\varphi}{2})} \right) & \text{if } \frac{\varphi}{2} \geq \frac{\pi}{4} \\ 0.01143R^4(\frac{\varphi}{2})^7 \left(1 - 0.3491(\frac{\varphi}{2})^2 + 0.045(\frac{\varphi}{2})^4 \right) & \text{if } \frac{\varphi}{2} < \frac{\pi}{4}. \end{cases} \quad (12)$$

I_{Ci} , the second moment of area of the inner circular segment A_i (see Fig. 7b) is defined by (12) with $R = R_i$ and $\varphi = \varphi_i$, whereas I_{Co} , the second moment of area of the outer circular segment A_o is defined by (12) with $R = R_o$ and $\varphi = \varphi_o$. Using (12), the second moment of area of these segments with respect to the center of the tube is obtained using the parallel-axis theorem:

$$\begin{cases} I_i &= I_{Ci} + A_i C_i^2 \\ I_o &= I_{Co} + A_o C_o^2 \end{cases} \quad (13)$$

with A_i , A_o , A_T , C_i and C_o , the areas and centroids, respectively, which follow from the geometry of the beam (Fig. 7b):

$$\begin{cases} A_i &= \frac{1}{2} R_i^2 (\varphi_i - \sin(\varphi_i)) \\ A_o &= \frac{1}{2} R_o^2 (\varphi_o - \sin(\varphi_o)) \\ A_T &= A_o - A_i. \end{cases} \quad (14)$$

Because I_o and I_i have now the same reference, i.e. the center of the tube, they can be used to calculate the second moment of area of the flexible beam determined by the difference between the outer and inner area:

$$I_{CA} = I_{Co} - I_{Ci}. \quad (15)$$

Now that I_{CA} has been defined, it can be used in (10) in order to derive the large displacement equations of the beams.

2.1.3. Large displacement of the flexible beams

Using the following expression for the bending curvature of the beam:

$$\frac{1}{\rho(s)} = \frac{d\theta(s)}{ds} \quad (16)$$

with $\theta(s)$, the angle between the positive x-axis and the tangent to the neutral axis at the specific point s (Fig. 5). By combining Eqs. (10) and (16) we can obtain:

$$\frac{d\theta(s)}{ds} = \frac{M}{E_{eq}(\epsilon_{max})I_{CA}}, \quad (17)$$

where $\theta = 0$ is chosen as initial condition at the base of the beam, thus for $s = 0$. The value of $\theta(s)$ can be found by integration on s :

$$\theta(s) = \frac{M}{E_{eq}(\epsilon_{max})I_{CA}} s. \quad (18)$$

The following geometric relations can be used to obtain the Cartesian coordinates of any point situated on the neutral axis of the deflected beam at any arc length s from the base.

$$\begin{cases} \frac{dx}{ds} &= \cos(\theta(s)) \\ \frac{dy}{ds} &= \sin(\theta(s)). \end{cases} \quad (19)$$

The position of the deformed top of the beam of a section j (indicated as x_{D_j} and y_{D_j} , with $j = 1$ in Fig. 5) can therefore be calculated by integrating over the beam length from $s = 0$ to $s = L_j$. For $x = 0$ and $y = 0$ as initial condition at the base of the beam, this gives:

$$x_{D_j} = \frac{E_{eq_j} I_{CA_j}}{M_j} \sin\left(\frac{M_j}{E_{eq_j} I_{CA_j}} L_j\right) \quad (20)$$

$$y_{D_j} = \frac{-E_{eq_j} I_{CA_j}}{M_j} \cos\left(\frac{M_j}{E_{eq_j} I_{CA_j}} L_j\right) + \frac{E_{eq_j} I_{CA_j}}{M_j}. \quad (21)$$

From (20) and (21), the transformation matrix that expresses the position and orientation of the frame 1 with respect to the frame 0 of a section j (Fig. 5) can be found as:

$$T_{1,j}^{0,j} = \begin{bmatrix} \cos(\theta_j(L_j)) & -\sin(\theta_j(L_j)) & 0 & x_{D_j} \\ \sin(\theta_j(L_j)) & \cos(\theta_j(L_j)) & 0 & y_{D_j} \\ 0 & 0 & 1 & 0 \\ 0 & 0 & 0 & 1 \end{bmatrix}. \quad (22)$$

Since the teeth do not undergo any deformation (hypothesis 2 in Appendix A), the tooth tip position of a section j (i.e. x_{tooth_j} and y_{tooth_j} , illustrated for $j = 1$ in Fig. 5) can be obtained by simple trigonometry, which gives:

$$\begin{bmatrix} x_{tooth_j} \\ y_{tooth_j} \\ 0 \\ 1 \end{bmatrix} = T_{1,j}^{0,j} \cdot \begin{bmatrix} 0 \\ l_{c_j} \\ 0 \\ 1 \end{bmatrix} = \begin{bmatrix} -l_{c_j} \sin(\theta_j(L_j)) + x_{D_j} \\ l_{c_j} \cos(\theta_j(L_j)) + y_{D_j} \\ 0 \\ 1 \end{bmatrix} \quad (23)$$

with $l_{c_j} = (R_o + C_{A_j})$, the distance between the tooth extremity and the neutral axis C_{A_j} , as shown in Fig. 5 for $j = 1$.

In order to choose the correct E_{eq} in Eq. (18), ϵ_{max} needs to be calculated. To do so, Eqs. (2) and (10) can be combined to form the following expression for a given flexible beam j :

$$M_j = \frac{E_{eq_j}(\epsilon_{max_j}) I_{CA_j} \epsilon_{max_j}}{y_{max_j}}, \quad (24)$$

where y_{max_j} is the location of the maximum strain, i.e. at the outer fiber (Fig. 7) of the beam j , and is equal to $R_o - C_{A_j}$. Eq. (24) is solved for a given input torque M_j to find ϵ_{max_j} by numerical methods.

2.2. Large displacement model of an arbitrary individual NiTi side-notched backbone section

In this subsection, the deformation model for an arbitrary section of the backbone is described. Three different cases are analyzed. First, the case of the most distal notch is discussed. This notch will behave differently from the others since its tooth portion serves as a lever to transmit the

moment to the beam portion. Second, all the other notches are considered. In this case, the bending moment is caused by the moment transferred from the upper sections. Third, the limit case is elaborated on, with the deformation being so large that the adjacent teeth come into contact with each other.

2.2.1. Deformation of the top section

If a force F_{app1} is applied to the first tooth by the wire, the flexible beam of the first top section will bend. This bending will induce a normal force between the wire and the tooth N_1 (Fig. 8) which, in turn, will induce friction f_1 (Fig. 8). Both N_1 and f_1 depend on the section bending θ_1 . Details about the calculation of N_1 and f_1 can be found in subsection 2.4. The torque M_1 applied to the beam end of the backbone section can therefore be expressed as:

$$M_1 = F_{app1}l_{c1} + N_1(\theta_1)\frac{h_{t1}}{2} + f_1(\theta_1)l_{c1}. \quad (25)$$

This torque, M_1 , can be used in Eqs. (20) and (21) in order to find the first tooth tip position by using (23).

2.2.2. Deformation of the next sections without contact

For each section, frames can be allocated to key points on the beam and tooth of the section. Four frames can be defined for a section j : frames $\{0, j\}$, $\{1, j\}$, $\{2, j\}$ and $\{3, j\}$ (Fig. 8).

The torque M_2 applied to the beam top of the second section is the sum of the torque M_1 and the effect of the bending of the second section, i.e. the effect of the normal force between the wire and the tooth N_2 and the consequent friction force f_2 (Fig. 8):

$$M_2 = M_1 + N_2(\theta_2)\frac{h_{t2}}{2} + f_2(\theta_2)l_{c2}. \quad (26)$$

By extending and generalizing this procedure, the torque M_j applied to the top beam of the j^{th} section can therefore be calculated as:

$$M_j = M_{j-1} + N_j(\theta_j)\frac{h_{tj}}{2} + f_j(\theta_j)l_{cj}. \quad (27)$$

By combining Eqs. (23) and (27), the position of the different j^{th} tooth extremities, i.e. x_{toothj} and y_{toothj} can be found.

2.2.3. Deformation in case of teeth contact

If the torque M_j , applied to the beam top of the j^{th} section, is large, the $(j+1)^{th}$ and the j^{th} teeth could touch each other (Fig. 9). In order to model this phenomenon, the limit torque M_{limitj} , causing the tooth of the j^{th} section to touch

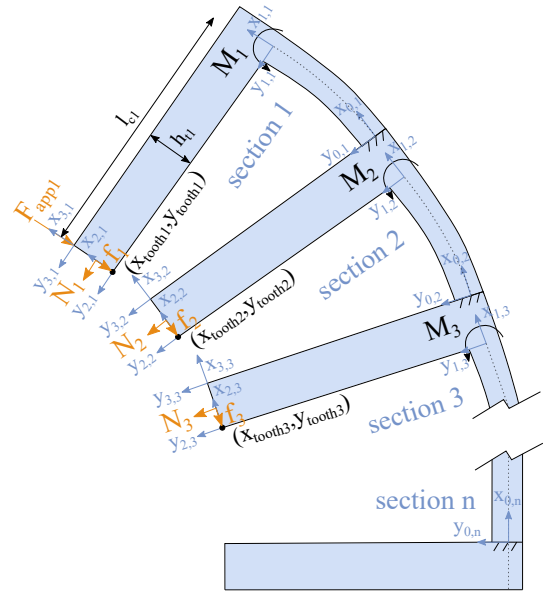


Figure 8: Force and torque distribution on the NiTi backbone to calculate the position of the tooth extremity of all the successive sections.

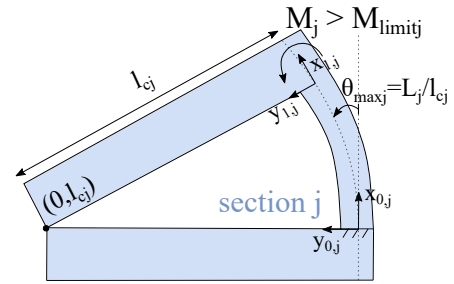


Figure 9: Side-notched backbone section j in case of teeth contact as a result of the bending moment M_j being larger than M_{limitj} .

the tooth of the $(j+1)^{th}$ teeth, can be found by imposing $x_{toothj} = 0$, and inserting Eq. (18) in (23), which gives:

$$M_{limitj} = \frac{E_{eq} I_{CAj}}{l_{cj}}. \quad (28)$$

If the torque M_j is larger or equal to M_{limitj} , then x_{toothj} and y_{toothj} are respectively set equal to 0 and l_{cj} in frame $\{1, j\}$. The bending angle is set to $\theta_{maxj} = L_j / l_{cj}$, which can be found by inserting Eq. (28) in (18).

2.3. Large displacement model of a NiTi side-notched backbone

In order to obtain the overall shape of the NiTi backbone, each section can be concatenated using transformation matrices linking frames $\{0, j-1\}$ and $\{0, j\}$. The transformation matrix that expresses the position and orientation of frame $\{0, j-1\}$ with respect to frame $\{0, j\}$ (Fig. 8) is given

by:

$$T_{0,j-1}^{0,j} = \begin{bmatrix} \cos(\theta_j) & -\sin(\theta_j) & 0 & x_{D_j} + h_{t_j} \cos(\theta_j) \\ \sin(\theta_j) & \cos(\theta_j) & 0 & y_{D_j} + h_{t_j} \sin(\theta_j) \\ 0 & 0 & 1 & 0 \\ 0 & 0 & 0 & 1 \end{bmatrix}. \quad (29)$$

By defining frame 0 (Fig. 8) of the most proximal section as the base frame (i.e, frame n), the overall shape of the instrument can be derived by identifying the beam end positions (the origins of frame 0 and 1 in Fig. 8) as well as the position of the teeth extremities (the origins of frame 2 and 3 in Fig. 8) for each section relative to the base frame.

The origin of frame $\{0, j\}$ is defined as

$$O_{0,j}^{0,n} = \prod_{m=j}^2 \left(T_{0,m-1}^{0,m} \right) \cdot \begin{bmatrix} 0 \\ 0 \\ 0 \\ 1 \end{bmatrix}. \quad (30)$$

The origin of frame $\{1, j\}$ is found as

$$O_{1,j}^{0,n} = \prod_{m=j}^2 \left(T_{0,m-1}^{0,m} \right) \cdot \begin{bmatrix} x_{D_j} \\ y_{D_j} \\ 0 \\ 1 \end{bmatrix}. \quad (31)$$

The origin of frame $\{2, j\}$ is found using (22):

$$O_{2,j}^{0,n} = \prod_{m=j}^2 \left(T_{0,m-1}^{0,m} \right) \cdot T_{1,j}^{0,j} \cdot \begin{bmatrix} 0 \\ l_{c_j} \\ 0 \\ 1 \end{bmatrix}. \quad (32)$$

Finally, the origin of frame $\{3, j\}$ is defined by

$$O_{3,j}^{0,n} = \prod_{m=j}^2 \left(T_{0,m-1}^{0,m} \right) \cdot T_{1,j}^{0,j} \cdot \begin{bmatrix} h_{t_j} \\ l_{c_j} \\ 0 \\ 1 \end{bmatrix}. \quad (33)$$

In order to calculate the overall bending angle of the side-notched backbone, the bending angle of each notch, θ_j , can simply be added. The overall bending angle can therefore be expressed as:

$$\Theta = \sum_{j=1}^n \theta_j. \quad (34)$$

All the θ_j can easily be found by using Eq. (18).

Eqs. (25), (27) and (28) can then be used to compute the bending angles of each notch, θ_j .

2.4. Friction between the wire and the backbone

The force F_{app1} applied to the first tooth extremity differs from the proximal force applied to the wire by an external actuator. This difference is due to friction resulting from the normal force applied by the pull wire to the backbone teeth. In order to model this phenomenon, the Capstan equation is proposed. This equation has, amongst others, been used to model the tendon transmission system of robotic fingers [19]. The Capstan equation relates the incoming tension force F_1 to the outgoing tension force F_2 (with $F_2 > F_1$) of a flexible cable wound around a drum (Fig. 10a) [20]. Due to the interaction of frictional forces and tension, the tension is different on each side of the drum. This difference is characterized by:

$$F_2 = F_1 e^{\mu\beta} \quad (35)$$

with μ , the friction coefficient of the cable on the drum, and β the slip angle (Fig. 10a). The Capstan equation (35) can be applied to one section of the notched backbone. Indeed, when the wire is tensioned and the backbone section deforms, the wire presses on the backbone's inner wall and follows its shape. Locally, this can be approached like a circular arc (Fig. 10b), as the circle defined by this circular arc can be seen as the Capstan drum of radius R . The slip angle is the angle delimiting the tooth of the j^{th} section, i.e. the circle segment delimited by the points $O_{3,j}^{0,j}$ and $O_{2,j}^{0,j}$ in Fig. 10b.

The normal force N_j applied by the wire to the backbone j^{th} tooth (Fig. 10b) can be calculated by summing the forces in the y -direction in Fig. 10a:

$$N_j(\theta_j) = F_{r_j} \beta_j(\theta_j), \quad (36)$$

where F_{r_j} represents the tension in the rope below the j^{th}

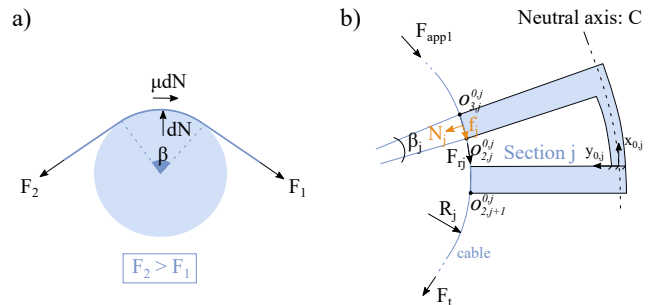


Figure 10: Friction model based on the Capstan equation; a) illustration of a capstan drive mechanism; b) Capstan drive applied to a notched backbone section j .

tooth (Fig. 10b). This force can be calculated using Eq. (35) in its static form (i.e. when $f \leq \mu N$):

$$F_{r_j} \geq F_{r_{j-1}} e^{\mu_s \beta_j}, \quad (37)$$

where μ_s is the coefficient of static friction and $F_{r_0} = F_{app1}$. The static friction force applied by the wire to a backbone tooth can therefore be expressed as:

$$f_j(\theta_j) \leq \mu_s N_j(\theta_j). \quad (38)$$

Eqs. (36) and (38) depend on β_j :

$$\beta_j = h_{t_j} / R_j, \quad (39)$$

where h_{t_j} is the thickness of the j^{th} tooth and R_j is the radius of the circle passing through three teeth extremities of section j , namely the points $O_{3,j}^{0,j}$, $O_{2,j}^{0,j}$ and $O_{2,j+1}^{0,j}$ in Fig. 10b. The coordinates of these three points can be derived as follows in the frame of the j^{th} section:

$$O_{3,j}^{0,j} = T_{1,j}^{0,j} \cdot \begin{bmatrix} h_{t_j} \\ l_{c_j} \\ 0 \\ 1 \end{bmatrix} \quad (40)$$

$$O_{2,j}^{0,j} = T_{1,j}^{0,j} \cdot \begin{bmatrix} 0 \\ l_{c_j} \\ 0 \\ 1 \end{bmatrix} \quad (41)$$

$$O_{2,j+1}^{0,j} = \begin{bmatrix} -h_{t_{j+1}} \\ l_{c_{j+1}} \\ 0 \\ 1 \end{bmatrix}. \quad (42)$$

β_j is a function of θ_j by using Eqs. (40), (41) and (42).

θ_j is a function of M_j by (18). Therefore, by inserting Eqs. (36) and (38) in (27), M_j is found using Matlab's *fzero* function (MathWorks, Natick, USA) with a termination tolerance of $2.2204e-16$ (default value) and an initial point equal to 0.

A force F_t applied proximally to the wire creates a reaction force F_{app1} on the tooth extremity of the first section that is smaller than F_t because all the friction forces f_j work on the wire and oppose the wire's movement (Fig. 10). The equivalent slip angle of the entire backbone is obtained by summing the slip angles of the individual sections. F_t is therefore linked to F_{app1} by using the Capstan equation in its static form:

$$F_t \geq F_{app1} e^{\mu_s \sum_{j=1}^n \beta_j} \quad (43)$$

The computational method to find F_t in function of F_{app1} is described in detail in Algorithm 1 and goes as follows. From a known tension force F_t , F_{app1} needs to be found in order to apply the proposed static model (Eqs. (25) - (27)). However, the angles β_j depend on the bending angles of each notch, θ_j , and therefore on F_{app1} . The angles β_j in Eq. (43) will therefore be expressed as a function of F_{app1} . Eq. (43) is solved using the Matlab's *fsolve* function (MathWorks, Natick, USA) with a Levenberg-Marquardt optimization algorithm, a termination tolerance on the function value of $1e-6$, a maximum number of iterations of 400, and an initial point equal to F_t . More specifically, β_j is a function of θ_j by using Eqs. (40), (41) and (42). θ_j is a function of M_j by using (18), and M_j is a function of F_{app1} by using Eqs. (25), (27) and (28). Eq. (25) is used for the first notch. For the other notches, either Eq. (27) or (28) are used depending on the state of the previous notch. If M_{j-1} is larger than $M_{limit_{j-1}}$, Eq. (28) will be used. Otherwise Eq. (27) is used.

3. Experiments

In order to evaluate and validate the complete static model for large displacements of side-notched tube instruments with integrated friction modeling, four NiTi samples were manufactured in-house using wire Electrical Discharge Machining (EDM) (Fig. 11). The first sample was manufactured from a 2.3mm outer diameter, 1.8mm inner diameter tube with six equal depth notches. The second, third and fourth samples were machined from a 2.3mm outer diameter, 2mm inner diameter tube with equal, increasing-size and decreasing-

Algorithm 1: Expressing F_t in function of F_{app1}

```

Input :  $F_t$ 
 $j \leftarrow 1$ ;
while  $j \leq n$  do
    if  $j = 1$  then
         $M_j = F_{app1} l_{c_j} + N_j(\theta_j) \frac{h_{t_j}}{2} + f_j(\theta_j) l_{c_j}$ ;
    else
        if  $M_{j-1} > M_{limit_{j-1}}$  then
             $M_j = \frac{E_{eq_j} l_{CA_j}}{l_{c_j}}$ ;
        else
             $M_j = M_{j-1} + N_j(\theta_j) \frac{h_{t_j}}{2} + f_j(\theta_j) l_{c_j}$ ;
        end
    end
     $\theta_j = \frac{M_j L_j}{E_{eq_j} (\epsilon_{max_j}) l_{CA_j}}$ ;
     $\beta_j \leftarrow Eq.(40), (41), (42) \leftarrow Eq.(22)$ ;
     $j \leftarrow j + 1$ ;
end
 $F_t = F_{app1} e^{\mu_s \sum_{j=1}^n \beta_j}$ ;
Output:  $F_t(\beta_j(\theta_j(M_j(F_{app1}))))$ 
    
```

size depth notches respectively (Table 2). Note that choosing larger notch depths for the distal notches than for the proximal ones allows reaching small bending radii during bending, since the distal notches will bend first. The resulting backbone is therefore promising for limited workspace surgery. Even if preferential distal bending is observed when using equal-depth notches, this property is amplified when the depth of the distal notches is larger. This technique, called *tip-first bending*, was introduced by Swaney *et al.* [21]. However, until now, no model has been introduced that takes into account non-constant curvature bending to model *tip-first bending* backbones.

The employed NiTi was heat-treated prior to manufacturing. More specifically, the sample was annealed at 550°C for 10min. This heat treatment causes a decrease of the stress plateau by approximately 20% (Fig. 12) [22], which, in turn, leads to a decrease in the load required to bend the NiTi backbone.



Figure 11: Samples used to evaluate the static model, with enlargement of the perforation used to attach the wire to the tube. 1. 2.3mm outer diameter, 1.8mm inner diameter equal notches backbone; 2. 2.3mm outer diameter, 2mm inner diameter equal notches backbone; 3. 2.3mm outer diameter, 2mm inner diameter increasing-size notches backbone; 4. 2.3mm outer diameter, 2mm inner diameter decreasing-size notches backbone.

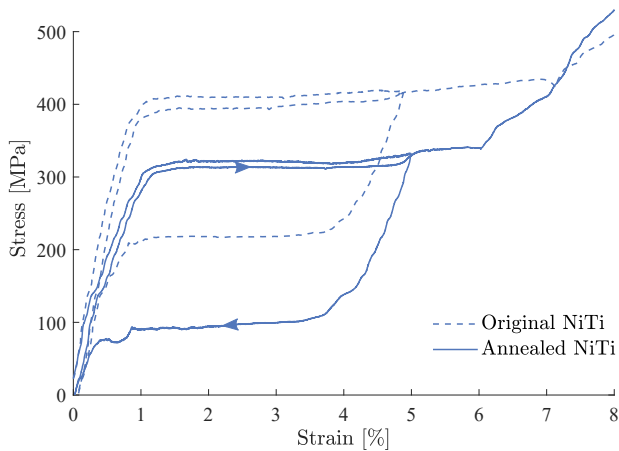


Figure 12: Stress-strain tensile curve of an annealed and an original NiTi tube sample.

Table 2

Notch depth g_j and length L_j and tooth thickness h_j of the four samples

j	Sample 1	Sample 2	Sample 3	Sample 4
	(g_j, L_j, h_j) [mm]			
1	(2.14, 1.14, 2.19)	(2.15, 1.11, 1.7)	(1.94, 1.06, 1.87)	(2.25, 1.24, 2.16)
2	(2.14, 1.14, 0.77)	(2.15, 1.18, 0.67)	(2.02, 1.07, 0.76)	(2.13, 1.19, 0.74)
3	(2.14, 1.17, 0.75)	(2.16, 1.18, 0.69)	(2.05, 1.21, 0.72)	(2.05, 1.24, 0.73)
4	(2.15, 1.3, 0.79)	(2.13, 1.28, 0.76)	(2.08, 1.14, 0.74)	(2.01, 1.2, 0.7)
5	(2.08, 1.29, 0.77)	(2.13, 1.2, 0.69)	(2.12, 1.23, 0.71)	(1.89, 1.17, 0.78)
6	(1.97, 1.32, 0.81)	(2.03, 1.21, 0.76)	(2.14, 1.23, 0.76)	(1.86, 1.12, 0.74)

3.1. Set-up

In order to evaluate the static model experimentally, the backbone shape was recorded in function of the force applied to the wire. To do so, the set-up depicted in Fig. 13 was used. The four NiTi samples (Fig. 11) were clamped onto a support piece with a hole drilled into so that a wire can freely pass through the backbone. The wire, a 200 μ m diameter stainless-steel single thread cable, was attached to a load cell BCM 16687(S) 1kg (BCM sensor, Antwerpen, Belgium) at one end. The other end of the wire was attached to the most distal tooth of the backbone by making a simple knot around a small hole manufactured in the first tooth (Fig. 11). The load cell was clamped on a linear stage M-423 (Newport Corporation, California, USA). The force applied to the wire could be regulated using a micrometer SM-25 (Newport Corporation, California, USA) mounted on the linear slide. The force value was measured using a cRIO-9067 and a Labview module NI9237 (National Instruments, Texas, USA). In order to experimentally register the points $O_{2,j}^{0,n}$ and $O_{3,j}^{0,n}$ (Fig. 8), an Andonstar V160 digital microscope was used (Andonstar, Guang Dong, China). The microscope was first calibrated using the open source 'Camera Calibration Toolbox for Matlab'. Then, a Matlab (MathWorks, Natick, USA) program was developed to compute the location of the manually selected points on the picture. The accuracy and precision of this manual selection point program was measured to be 0.05mm and 0.17mm, respectively. By applying an arbitrary force to the pull wire and manually selecting the points' position $O_{2,j}^{0,n}$ and $O_{3,j}^{0,n}$ on the bent backbone, the side-notched instrument bending behaviour could be experimentally measured and compared to the static model.

3.2. Model Parameters definition

The dimensions of the notches of the four samples are reported in Table 2. Due to inaccuracies in the manufacturing process, all these dimensions were precisely remeasured using the open access image processing program *Image J*. In Table 2, the notch number corresponds to the parameter j defined in subsection 2.2. Note that the depth of some notches is so large that the flexible beam cross section becomes a circular segment. These notches are characterized by a depth $g_j \geq R_o + R_i$. For these notches, the second moment of area

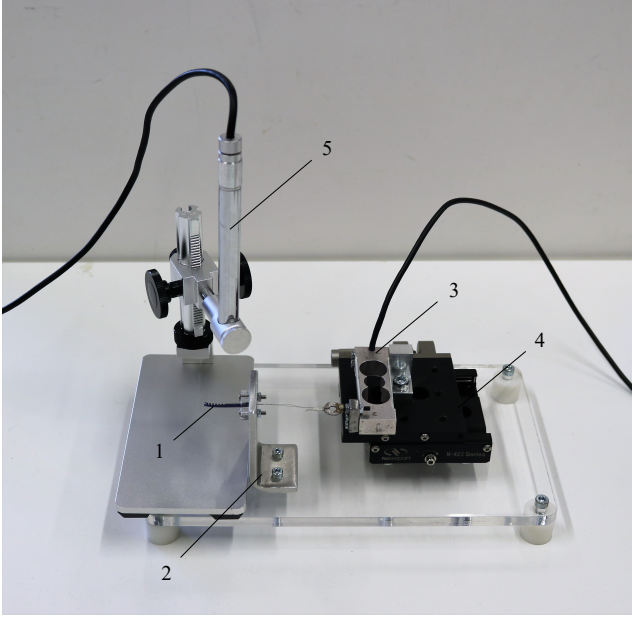


Figure 13: Set-up used to evaluate the static model of the NiTi side-notched backbone. 1. sample; 2. sample support piece; 3. load cell; 4. linear stage; 5. microscope.

of a circular segment was used (Fig. 7a). The static coefficient of friction was experimentally obtained by fitting the model curve on the experimental one.

The material properties of the used NiTi tubes were also measured. More specifically, the stress-strain curve of the used NiTi was measured using a universal testing machine Instron 5567 (Instron, Massachusetts, USA). The hysteresis curve and the load to failure test were obtained by using a speed of 0.4mm/min for two samples, one annealed and one original, coming from the same production tube (Fig. 12).

Based on the experimental curve of the annealed NiTi, the equivalent, strain dependent, linear elastic modulus E_{eq} can be calculated in function of ϵ_{max} . Eq. (24) can then be used to find the corresponding ϵ_{max} to a torque input M_j , which can therefore lead to an E_{eq} matching the deformation.

In addition to being superelastic, NiTi shows hysteresis during tension and release (Fig. 12). Thus, in order to calculate E_{eq} , the loading and unloading cases need to be analyzed.

3.2.1. E_{eq} - loading case

By solving (7) for different values of ϵ_{max} , the curve of $E_{eq}(\epsilon_{max})$ can be obtained (Fig. 14). From 0 to 1.5% strain, the E_{eq} varies around 3.4×10^4 MPa. This strain range corresponds to the linear domain of the NiTi. However, it is important to note that the slope of the experimental stress-strain curve slightly varies in this range, therefore, the E_{eq} varies accordingly. Between 1.5 and 6.5% strain, which corresponds to the plateau range of the NiTi, E_{eq} decreases. From 6.5% strain, E_{eq} is constant around 0.75×10^4 MPa

since the stress-strain curve of the NiTi is linear once again.

3.2.2. E_{eq} - unloading case

Since NiTi shows hysteresis, the NiTi unloading curve needs to be used to calculate the E_{eq} of the unloading case. The unloading E_{eq} is not only dependent on the strain, but also on the maximum strain reached just before unloading. From this specific strain, the stress-strain profile of the backbone flexible beam section takes the form of the loading curve with a maximum strain corresponding to the unloading curve (decreasing blue curves in Fig. 15)) in accordance with (2). Those stress-strain profiles were used to calculate the integral in (7), and the unloading E_{eq} could be obtained in function of ϵ_{max} and ϵ_{max} before unloading (b.u.) (Fig. 14). In Fig 14 E_{eq} is showed for ϵ_{max} b.u. equals to 10%. If ϵ_{max} b.u. < 10%, it is assumed that E_{eq} decreases at the same pace as E_{eq} for ϵ_{max} b.u. = 10% until the unloading E_{eq} curve is reached (Fig. 14).

3.3. Results

The experiments were conducted five times for different applied forces ranging from 0 to 2N for the first sample, 0 to 1.2N for the second, and 0 to 4N for the third and fourth samples. In order to test the model's validity for the unloading case, an unloading test was also performed on the second sample in which loads ranging 1.2 to 0N were applied onto the pull wire.

The model was implemented in Matlab R2017a (Math-Works, Natick, USA) and can calculate the backbone position for one tension force in 1.87s on average using a processor Intel(R) Core(TM)i7-7600U and a CPU of 2.8GHz. This test was conducted by using the program coded in Matlab with 50 randomly applied tension forces. The execution time of the program was not the focus of this work and is currently

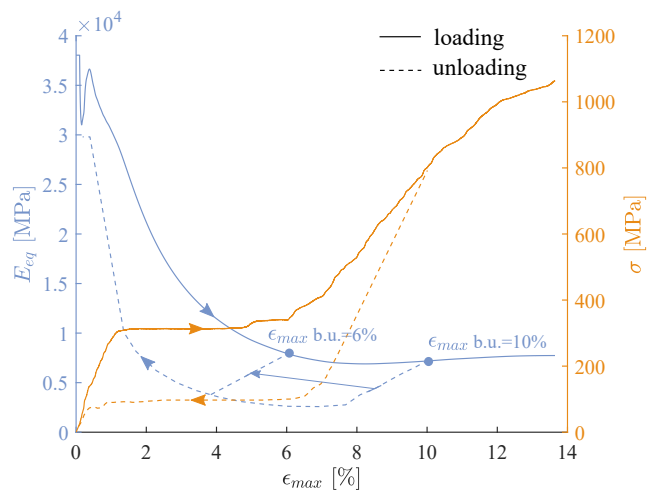


Figure 14: E_{eq} obtained by solving (7) for the loading and unloading curve (blue) and stress-strain loading and unloading curve of the NiTi (orange) with ϵ_{max} before unloading (b.u.) equal to 10%. Example of E_{eq} for ϵ_{max} b.u. equal to 6%.

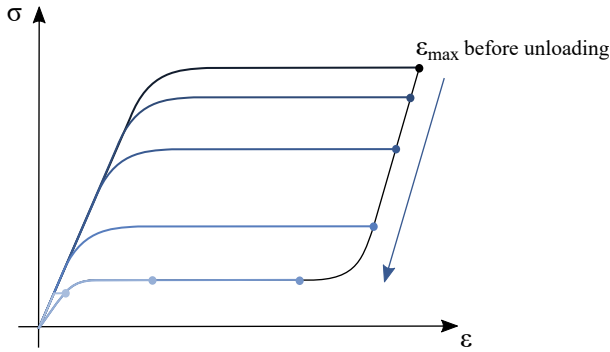


Figure 15: Stress-strain profiles (blue curves) of a backbone flexible beam section during unloading.

too high for use in a real-time control scheme. However, there is still some room for speed up e.g. by coding the model in a lower level language.

Figure 16 depicts the bending angle and the notch positions of the four different samples for different forces applied to the pull wire. The figure shows both the angles and positions that were obtained experimentally and those predicted by the static model. For the bending angles, the mean and standard deviation (SD) of the five experimental tests are plotted and the RMSE between the mean of the experiments and the model is indicated. For the notches positions (i.e. the points $O_{2,j}^{0,n}$ and $O_{3,j}^{0,n}$ defined in Section 2), the mean position over the five tests is depicted and the mean RMSE of the notch positions is also indicated. In order to calculate this position RMSE, the mean of the Euclidean distance between the 12 modeled and experimental points was considered to calculate the RMSE for different applied forces. The RMSE was then normalized in function of the height of the NiTi backbone at rest.

For the first sample, a static friction coefficient of 0.31 shows the best results. To draw a comparison, Kusy et al. [23] reported a coefficient of dry static friction between stainless-steel dental brackets and NiTi wires equal to 0.302. The model can estimate its bending angle with an RMSE of 3.1% and the position of its notches with a mean RMSE of 2.7% over a range of 2N applied force.

The model approximates the bending angle of the second sample in its loading phase with an RMSE of 6.1%, and the notch positions with a mean RMSE of 4.8% over a range of 1.2N applied force. For these results, a static friction coefficient of 0.42 was chosen. The model shows some discrepancy at small applied forces (Fig. 16B). In the unloading phase, the model predicts the deflection angle with an RMSE of 5.7% and the notch positions with a mean RMSE of 5%. Deflection angle deviations similar to those of the loading case are observed at small applied forces (Fig. 16C). By comparing the deflection angles of both loading and unloading cases (Fig. 16B and C), the hysteresis intrinsic to the NiTi material becomes noticeable. One can see that the

tube starts straightening only after reducing the load below 1N.

An RMSE of 4.5% was calculated for the bending angles of the third sample. The model approximated the notch positions with a mean RMSE of 3% across a range of 4N applied force. For the third sample, a static friction coefficient of 0.2 showed the best results.

Finally, a static friction coefficient of 0.2 was chosen for the last sample. The model replicates the bending angle of the fourth sample with an RMSE of 3.7% and the position of its notches with a mean RMSE of 2.5% across a range of 4N applied force.

4. Discussion

The developed static model can predict the bending angle and the notch positions of a NiTi side-notched backbone with a reasonable RMSE across a large bending angle range (i.e. up to 180°), even for unequally sized notches. This model, computing the deformation of each notch individually and using an equivalent linear E-modulus to model the superelasticity of the material, addresses the limitations of the currently existing models which can only model the deformation of NiTi backbones with identical notches up to maximum 90° [15, 8]. However, a couple of factors influence the accuracy of the proposed model, like the equivalent linear E-modulus and the friction coefficient between the wire and the NiTi backbone. In this section, these factors as well as their effect on the static model are discussed. The integration of such a model in the development framework of steerable instruments for constrained workspace surgery is also discussed.

4.1. Equivalent linear E-modulus

The equivalent linear E-modulus represents a way to deal with the superelasticity of the material while being able to use linear deformation equations. This equivalent linear E-modulus (E_{eq}) is an approximation of the material properties at a given elongation. Therefore, inaccuracies are expected in the NiTi backbone deflection especially at higher strain (i.e. above 1.5%), where the deformation is no longer linear. In the unloading case, in which the equivalent linear E-modulus does not only depend on the strain but also on the maximum strain reached just before unloading, inaccuracies may arise due to the assumption that E_{eq} decreases at the same pace as E_{eq} for ϵ_{max} b.u. = 10% until the unloading E_{eq} curve is reached (Fig. 14).

4.2. Friction coefficient

The coefficient of friction depends on various factors such as the microstructure of the different materials, the surface finish (manufacturing history, process parameters) and the geometry. Sample 1 (2.3mm outer diameter and 1.8mm inner diameter) comes from a different batch than samples 2, 3 and 4 (2.3mm outer diameter and 2mm inner diameter).

Model of Side-Notched Tubes

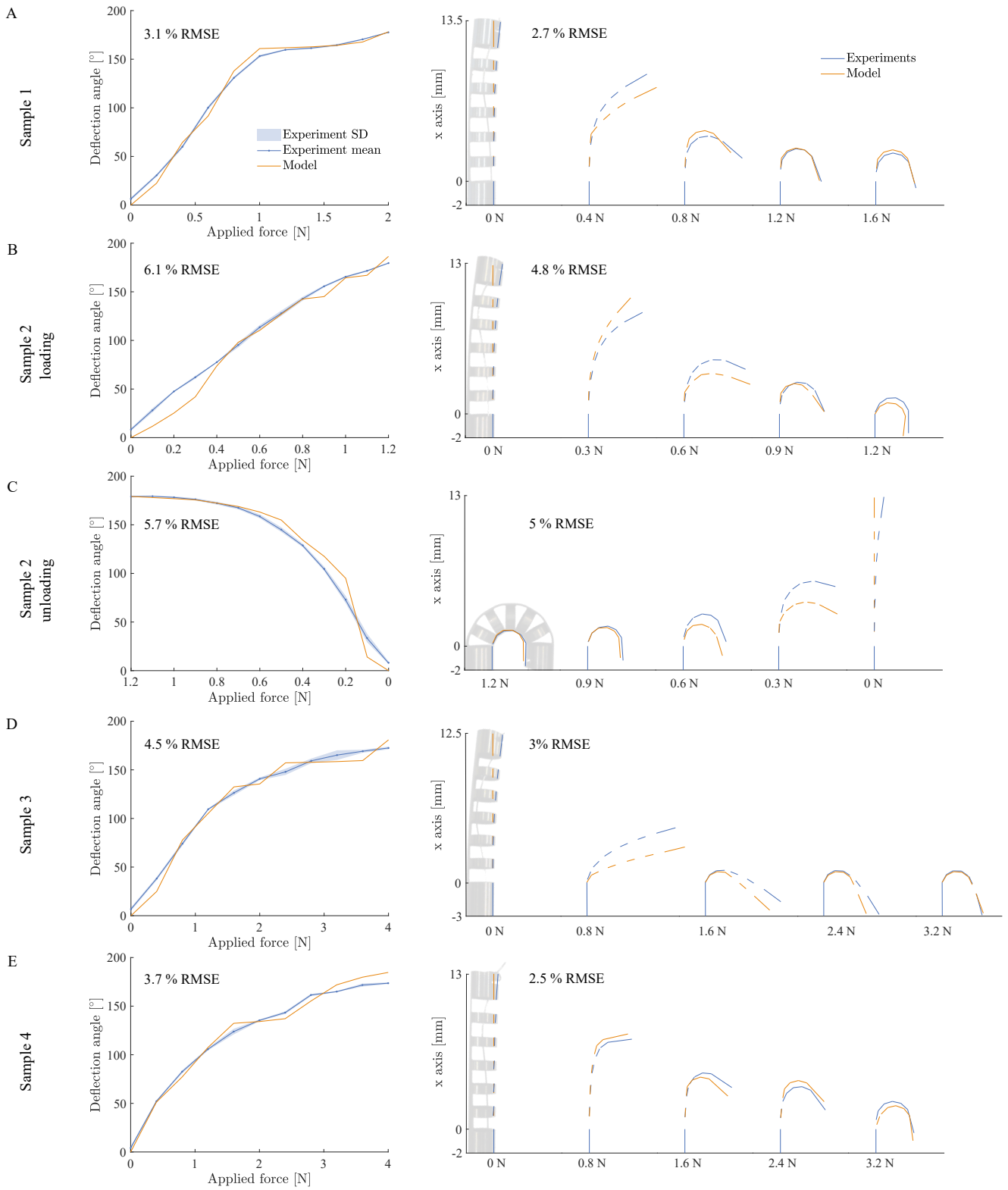


Figure 16: Comparison of the model's and experimental NiTi side-notched backbone's bending angle Θ (left) and notch positions (right) for different forces applied to the pull wire; A. first sample: 2.3mm outer diameter, 1.8mm inner diameter backbone with equal notches; B. second sample: 2.3mm outer diameter, 2mm inner diameter backbone with equal notches (loading case); C. second sample (unloading case); D. 2.3mm outer diameter, 2mm inner diameter backbone with increasing-size notches; E. 2.3mm outer diameter, 2mm inner diameter backbone with decreasing-size notches.

Moreover, all the samples have been heat-treated together. Since Sample 1 has a larger wall thickness than the other samples, Sample 1 potentially presents a different microstructure after heat-treatment than the rest of the samples. Therefore, a different coefficient of friction was found for Sample 1 (0.31) compared to the rest of the samples.

In order to manufacture the notches in the samples, the wire-EDM manufacturing technique was used. With wire-EDM, the material microstructure is modified locally at the cutouts. Samples 2, 3, and 4 have a different cutout geometry (see Table 2). Therefore, the microstructure profile along each tube (Sample 2, 3 and 4) is expected to be different. That is why a different friction coefficient was found for Sample 2 (0.42) than for Sample 3 and Sample 4 (0.2). Eq. (37) was used to model the friction. This equation was used with an equality to plot the results. The coefficient of static friction μ_s was chosen by fitting the model on the experiments. By doing so, it appeared that the model for Sample 3 and 4 showed results that were the closest to the experimental ones with a friction coefficient of 0.2 for both samples.

Note that without friction modeling, the RMSE of the model deflection angle would increase by 17.6% on average. This observation forms a strong motivation as to why friction modeling is needed.

4.3. Model integration

The proposed static model can be used to design and control steerable surgical instruments consisting of a NiTi side-notched backbone. Such instruments are particularly well suited for constrained workspace surgery, in which large bending angles and small bending radii are required. Vocal cord laser surgery is an example where acute bending can be very helpful. When removing polyps or a tumor on the vocal cords, the only view a surgeon has is from above the vocal cords through a straight rigid endoscope [24]. However, a view from underneath the vocal cords would help the surgeon to better identify the tumor and reduce the resection margins, which would increase the patient's chance of retaining some form of speech after surgery. A flexible NiTi side-notched instrument inserted through the buccal cavity down to underneath the vocal cords, equipped with a chip-on-tip camera, and capable of bending up to 180° would provide the surgeon with the desired extra view. The instrument needs to be able to bend within the dimensions of the larynx. The NiTi side-notched instrument can be designed for this purpose using the proposed static model by imposing a minimum bending angle and maximum bending radius computed from the patient's anatomy. The maximum bending angle of the side-notched backbone is found by adding the maximum bending angle of each backbone section. The maximum bending angle of one section is found by inserting (28) in (18). Hence, the maximum bending angle of the

backbone is given by,

$$\Theta_{max} = \sum_{j=1}^n \frac{L_j}{l_{c_j}}. \quad (44)$$

The parameters L_j and $l_{c_j} = C_A + R_o$, i.e. the height of the flexible *beam* portion and distance between the *beam* neutral axis and the extremity of the *tooth* portion respectively, can thus be chosen to meet the minimum required bending angle. In order for the instrument to bend within the lumen involved in the targeted surgical procedure, a condition can be expressed on the y component of the points $O_{2,j}^{0,n}$ and $O_{3,j}^{0,n}$, defined by (32) and (33). The y component of both points needs to be smaller than the diameter of this lumen for all loads applied to the pull wire. It is not straightforward to derive the geometric parameters meeting such a condition. However, the proposed static model does allow checking whether the bending properties are satisfied for a certain parameter choice.

Vocal cord laser surgery is only one of the many concrete applications in which large bending of thin steerable instruments in constrained spaces is necessary. Other examples are inspection and/or tumor removal in the maxillary sinus cavity via the nasal cavity, endoscopic skull base surgery via the nasal cavity, and endoscopic middle ear surgery. This way, the developed static model can find direct application in the design and control of NiTi side-notched tube instruments used in these and other surgical procedures in which a surgeon needs to maintain high dexterity in a constrained space.

5. Conclusions

This study has presented a static model capable of modelling large displacements of side-notched tube backbones made out of a superelastic material, i.e. NiTi. These type of instruments find application in constrained workspace surgery. The method, based on the beam deformation linear equations, makes it possible to calculate the successive deformation of each separate section of the backbone, taking the non-constant curvature bending of the backbone into account. The superelastic stress-strain curve of the material was approximated by an equivalent, strain dependent, linear elastic modulus. Such a technique makes it possible to model the NiTi in its elastic and superelastic regions. The study also adopts the capstan equation as a method to incorporate friction between the pull wire and the NiTi backbone. The static model can replicate the bending angle of the NiTi side-notched backbone with an RMSE as low as 3.1% and the backbone notch positions with an RMSE as low as 2.5%. The main concepts presented in this paper, i.e. the use of an equivalent, strain dependent, linear elastic modulus to represent the superelastic deformation of the NiTi, the calculation of the successive deformation of each separate section of the backbone and the friction model based on the Capstan equa-

tion can also be used in other NiTi notched tube designs.

Future work will focus on implementing the developed static model in order to control such an NiTi side-notched tube backbone. Applying this model in control schemes will allow to determine if the proposed static model is accurate enough to control this kind of backbone. Insertion of devices like a camera and surgical tools inside the backbone may alter the performance of the developed static model. That is why, in the future, dedicated experiments will need to be performed in order to quantify the effect of these inserted devices, and adapt the model if needed.

A. Justification of applicability of the seven hypotheses

This appendix provides some arguments to support the validity of the hypotheses that were made on the large displacement model for the superelastic material side-notched backbone. These hypotheses were listed in Section 2.

A.1. The superelasticity of the material can be approximated by an equivalent, strain dependent, linear elastic modulus

It was experimentally demonstrated in Section 3.3 that using such an equivalent, strain dependent, linear elastic modulus to approximate the NiTi stress-strain curve leads to an RMSE as low as 5.4° (3.1%) for the bending angle and an RMSE as low as 0.33mm (2.5%) for the position of each backbone notch across its entire bending range (0 to 180°). Therefore, it is reasonable to validate the use of an equivalent, strain dependent, linear elastic modulus to approximate the NiTi mechanical properties.

A.2. The backbone's teeth do not deform

In order to justify the applicability of this hypothesis, the second moment of area of the beam portion (Eq. (15)) was compared to that of the tooth portion.

Second moment of area of a tooth portion

The geometry of the cross section in the yz -plane of a tooth is an annulus (Fig. 4a). Its second moment of area with respect to its center is given by:

$$I_{tooth} = \frac{\pi}{4}(R_o^4 - R_i^4). \quad (45)$$

This expression can also be formulated with respect to the centroid of the flexible beam C_A (Fig. 7b):

$$I_{C_{tooth}} = \frac{\pi}{4}(R_o^4 - R_i^4) + \pi(R_o^2 - R_i^2)C_A^2 \quad (46)$$

with,

$$C_A = \frac{A_o C_o - A_i C_i}{A_o - A_i}. \quad (47)$$

Numerical example beam versus tooth second moment of area

For the first tube used in Section 3, i.e. a 2.3mm outer diameter and 1.8mm inner diameter tube, the calculated second moment of area of the tooth (2.4mm^4) represents more than eight times that of the beam (0.29mm^4) for a cutting depth of 2mm. For the second tube used in Section 3, i.e. a 2.3mm outer diameter and 2mm inner diameter tube, the second moment of area of the tooth (1.6mm^4) represents more than seven times that of the beam (0.21mm^4) for the same cutting depth as for the first example. The tooth portion will thus show substantial resistance to bending compared to the beam portion. Therefore, it is reasonable to assume that the tooth portion of the NiTi side-notched backbone will not deform under (un)loading from the pull wire.

A.3. The deformations are strictly planar

The bending deformation of the NiTi side-notched backbone was supposed to be strictly planar in the x - y plan (Fig. 4), since the wire is supposed to be placed at the backbone extremity in that same plan, and the notches are supposed to be precisely cut in the x - y plan. No significant lateral deformations were noted during experimentation.

A.4. The effect of shear stress on the deformation is neglected

This hypothesis falls within the hypotheses of the Euler-Bernoulli beam theory. This theory was used to predict the deflection of the flexible beam portions of the NiTi backbone. The Euler-Bernoulli beam theory for large displacement has shown to accurately predict the bending of various beams, even though it neglects shear stress [25, 26].

A.5. The buckling caused by the axial load on the beam portions can be neglected

The Euler's critical load at which a slender column will bend or buckle is given by the following formula:

$$P_{cr} = \frac{\pi^2 EI}{(KL)^2},$$

where, P_{cr} is the Euler's critical load, E is the Young's modulus of the column material, I is the minimum area moment of inertia of the cross section of the column, L is unsupported length of column and K is the column's effective length factor. In the case of the studied backbone, $P_{cr} \approx 1.47 \times 10^4 \text{N}$, which is significantly higher than the loads applied to the backbone in this study. Therefore, the axial loads will not cause the beam sections to bend or buckle. For this calculation, $K = 2$ was chosen in accordance with the recommended value in [27].

A.6. The normal forces applied by the cable to the backbone have a negligible effect on the bending of the beam sections

It was calculated that the deflection of the beam portion caused by the moments M_j was more than ten times higher than the deflection caused by the normal forces N_j applied

by the cable to the backbone. As a quick check, the small deflections of a cantilever beam subjected to an end load F and an end moment M , i.e. δ_F and δ_M , respectively, can be calculated:

$$\delta_F = \frac{FL^3}{3EI}$$

$$\delta_M = \frac{ML^2}{3EI}$$

From the model, values of the normal forces N_j and bending moment M_j were calculated and δ_F and δ_M were compared. Here is an example: $N = 0.38\text{N}$ and $M = 0.0058\text{N/m}$, gives $\delta_F = 2.4 \times 10^{-5}\text{mm}$ and $\delta_M = 4.8 \times 10^{-4}\text{mm}$. Therefore, it is considered that the normal forces applied by the cable onto the backbone have a negligible effect on the bending of the beam sections.

A.7. The friction present between the pull wire and the backbone are modeled using the Capstan equation

Section 4 demonstrates the importance of friction modeling. The results in accuracy of the quasi-analytical model that were presented in Section 3, i.e. an RMSE as low as 3.1% for the backbone bending angle and an RMSE as low as 2.5% for the backbone notch positions, allow to validate the use of the Capstan equation for friction modeling.

Acknowledgements

The authors would like to thank Katrien Schiepers for proof reading the article. This work was supported by the Belgian FWO [SB/1S98418N].

Author statement

Julie Legrand realized the static model, the experiments and the writing. Mouloud Ourak supervised the study and the writing, realized the heat treatment of the samples and the image processing algorithm to estimate the notch positions. Tom Vandebroek provided the samples and realized the heat treatment. Emmanuel Vander Poorten supervised the study and the writing. All authors have read and approved the current version of the paper. All authors have approved the order of authors listed in the paper.

Declaration of Competing Interest

We confirm that there are no known conflicts of interest associated with this publication and there has been no significant financial support for this work that could have influenced its outcome.

References

- [1] T. Kato, I. Okumura, H. Kose, K. Takagi, and N. Hata, "Extended kinematic mapping of tendon-driven continuum robot for neuroendoscopy," in *2014 IEEE/RSJ International Conference on Intelligent*

Robots and Systems, pp. 1997–2002, Sept. 2014. doi: 10.1109/IROS.2014.6942828.

- [2] A. Gao, J. P. Carey, R. J. Murphy, I. Iordachita, R. H. Taylor, and M. Armand, "Progress toward robotic surgery of the lateral skull base: Integration of a dexterous continuum manipulator and flexible ring curette," in *2016 IEEE International Conference on Robotics and Automation (ICRA)*, pp. 4429–4435, May 2016. doi: 10.1109/ICRA.2016.7487642.
- [3] M. Rox, K. Riojas, M. Emerson, K. Oliver-Butler, C. Rucker, and R. Webster, "Luminal robots small enough to fit through endoscope ports: Initial tumor resection experiments in the airways," in *Proceedings of the 2018 Hamlyn Symposium on Medical Robotics*, pp. 63–64, June 2018. doi: 10.31256/HSMR2018.32.
- [4] V. Agrawal, W. J. Peine, B. Yao, and S. Choi, "Control of cable actuated devices using smooth backlash inverse," pp. 1074–1079, May 2010. doi: 10.1109/ROBOT.2010.5509533.
- [5] A. Wadood, "Brief Overview on Nitinol as Biomaterial," *Advances in Materials Science and Engineering*, vol. 2016, p. 4173138, 2016. doi: 10.1155/2016/4173138.
- [6] H. Fischer, B. Vogel, W. Pflöging, and H. Besser, "Flexible distal tip made of nitinol (NiTi) for a steerable endoscopic camera system," *Materials Science and Engineering: A*, vol. 273-275, pp. 780–783, Dec. 1999. doi: 10.1016/S0921-5093(99)00415-3.
- [7] D. Wei, Y. Wenlong, H. Dawei, and D. Zhijiang, "Modeling of flexible arm with triangular notches for applications in single port access abdominal surgery," in *2012 IEEE International Conference on Robotics and Biomimetics (ROBIO)*, pp. 588–593, Dec. 2012. doi: 10.1109/ROBIO.2012.6491030.
- [8] K. W. Eastwood, H. Azimian, B. Carrillo, T. Looi, H. E. Naguib, and J. M. Drake, "Kinetostatic design of asymmetric notch joints for surgical robots," in *2016 IEEE/RSJ International Conference on Intelligent Robots and Systems (IROS)*, pp. 2381–2387, Oct. 2016. doi: 10.1109/IROS.2016.7759371.
- [9] K. W. Eastwood, P. Francis, H. Azimian, A. Swarup, T. Looi, J. M. Drake, and H. E. Naguib, "Design of a Contact-Aided Compliant Notched-Tube Joint for Surgical Manipulation in Confined Workspaces," *Journal of Mechanisms and Robotics*, vol. 10, pp. 015001–015001–12, Dec. 2017. doi: 10.1115/1.4038254.
- [10] Y. Chitalia, S. Jeong, K. K. Yamamoto, J. J. Chern, and J. P. Desai, "Modeling and control of a 2-dof meso-scale continuum robotic tool for pediatric neurosurgery," *IEEE Transactions on Robotics*, pp. 1–12, 2020. doi: 10.1109/TRO.2020.3031270.
- [11] M. D. M. Kutzer, S. M. Segreti, C. Y. Brown, M. Armand, R. H. Taylor, and S. C. Mears, "Design of a new cable-driven manipulator with a large open lumen: Preliminary applications in the minimally-invasive removal of osteolysis," in *2011 IEEE International Conference on Robotics and Automation*, pp. 2913–2920, May 2011. doi: 10.1109/ICRA.2011.5980285.
- [12] R. J. Murphy, Y. Otake, K. C. Wolfe, R. H. Taylor, and M. Armand, "Effects of tools inserted through snake-like surgical manipulators," *IEEE Engineering in Medicine and Biology Society. Annual Conference*, vol. 2014, pp. 6854–6858, 2014. doi: 10.1109/EMBC.2014.6945203.
- [13] L. Fichera, N. P. Dillon, D. Zhang, I. S. Godage, M. A. Siebold, B. I. Hartley, J. H. Noble, P. T. Russell, R. F. Labadie, and R. J. Webster, "Through the Eustachian Tube and Beyond: A New Miniature Robotic Endoscope to See Into the Middle Ear," *IEEE Robotics and Automation Letters*, vol. 2, pp. 1488–1494, July 2017. doi: 10.1109/LRA.2017.2668468.
- [14] J. Peirs, H. V. Brussel, D. Reynaerts, and G. D. Gerssem, "A flexible distal tip with two degrees of freedom for enhanced dexterity in endoscopic robot surgery," *Proceedings of the 13th Micromechanics Europe Workshop*, pp. 271–274, 2002.
- [15] P. A. York, P. J. Swaney, H. B. Gilbert, and R. J. Webster, "A Wrist for Needle-Sized Surgical Robots," *IEEE International Conference on Robotics and Automation*, vol. 2015, pp. 1776–1781, May 2015. doi: 10.1109/ICRA.2015.7139428.
- [16] P. Francis, K. W. Eastwood, V. Bodani, K. Price, K. Upadhyaya,

- D. Podolsky, H. Azimian, T. Looi, and J. Drake, "Miniaturized Instruments for the da Vinci Research Kit: Design and Implementation of Custom Continuum Tools," *IEEE Robotics Automation Magazine*, vol. 24, pp. 24–33, June 2017. doi: 10.1109/MRA.2017.2680547.
- [17] B. Zheng, B. Fu, T. A. Al-Tayeb, Y. F. Hao, and A. K. Qayumi, "Mastering instruments before operating on a patient: the role of simulation training in tool use skills," *Surgical innovation*, vol. 21, no. 6, pp. 637–642, 2014. doi: 10.1177/1553350614532533.
- [18] R. J. Roark, W. C. Young, and R. G. Budynas, *Roark's formulas for stress and strain*. New York: McGraw-Hill, 7th ed., 2002.
- [19] M. Kaneko, M. Wada, H. Maekawa, and K. Tanie, "A new consideration on tendon-tension control system of robot hands," in *Proceedings. 1991 IEEE International Conference on Robotics and Automation*, pp. 1028–1033, IEEE, 1991.
- [20] J. H. Jung, T. J. Kang, and J. R. Youn, "Effect of bending rigidity on the capstan equation," *Textile research journal*, vol. 74, no. 12, pp. 1085–1096, 2004. doi: 10.1177/004051750407401210.
- [21] P. J. Swaney, P. A. York, H. B. Gilbert, J. Burgner-Kahrs, and R. J. Webster, "Design, Fabrication, and Testing of a Needle-Sized Wrist for Surgical Instruments," *Journal of Medical Devices*, vol. 11, pp. 0145011–0145019, Mar. 2017. doi: 10.1115/1.4034575.
- [22] X. Yan and J. Van Humbeeck, "Effect of Annealing on Strain-Temperature Response under Constant Tensile Stress in Cold-Worked NiTi Thin Wire," *Smart Materials Research*, vol. 2011, pp. 1–6, 2011. doi: 10.1155/2011/160927.
- [23] R. P. Kusy, J. Q. Whitley, and M. J. Prewitt, "Comparison of the frictional coefficients for selected archwire-bracket slot combinations in the dry and wet states," *The Angle Orthodontist*, vol. 61, no. 4, pp. 293–302, 1991. doi: 10.1043/0003-3219(1991)061<0293:COTFCF>2.0.CO;2.
- [24] Y. P. Krespi and C. J. Meltzer, "Laser surgery for vocal cord carcinoma involving the anterior commissure," *Annals of Otolaryngology & Laryngology*, vol. 98, no. 2, pp. 105–109, 1989. doi: 10.1177/000348948909800204.
- [25] M. Brojan, T. Videnic, and F. Kosel, "Non-prismatic Non-linearly Elastic Cantilever Beams Subjected to an End Moment," *Journal of Reinforced Plastics and Composites*, vol. 26, pp. 1071–1082, July 2007. doi: 10.1177/0731684407079346.
- [26] H. Tari, "On the parametric large deflection study of euler-bernoulli cantilever beams subjected to combined tip point loading," *International Journal of Non-Linear Mechanics*, vol. 49, pp. 90–99, 2013. doi: 10.1016/j.ijnonlinmec.2012.09.004.
- [27] J. M. Gere and S. P. Timoshenko, "Mechanics of materials, ed." *Boston, MA: PWS*, 1997.



Julie Legrand received the MSc degree in Electromechanical Engineering with option Mechatronics from the Université Catholique de Louvain, Louvain-la-neuve, Belgium, in 2017. She is currently working toward a Ph.D. degree in robot-assisted surgery with the Katholieke Universiteit Leuven, Leuven, Belgium. Her research interests include surgical instrument design and control and miniature sensors and actuators development.



Mouloud Ourak holds a Ph.D. in Automation and Robotics from the Université de Franche-Comté in 2016 and a MS. degree in Robotics and Vision from the Université de Montpellier in 2013, in France. Since 2017, he is with the Katholieke Universiteit Leuven in the PMA Department at RAS group as a postdoctoral researcher (Leuven, Belgium). Currently, his research activities are related to surgical micro-robotics (actuators and control laws), vision and visual servoing.



Tom Vandebroek graduated with an MASc degree in Mechanical Engineering with a focus on biomechanics from the Université de Liège, Belgium in 2016. He is currently pursuing a Ph.D degree in robot-assisted surgery at the Katholieke Universiteit Leuven, Belgium. His research involves developing robots for single-port access surgery as well as low-profile add-ons to augment the capabilities of existing surgical instruments.



Emmanuel Vander Poorten (Ph.D, 2007 Kyoto University, Japan) is currently an Assistant Professor at the Mechanical Engineering Department at KU Leuven, Belgium. He is coordinator of the Robot-Assisted Surgery group, founder of CRAS, the Joint Workshop on New Technologies for Computer/Robot Assisted Surgery and Steering Board Member of ACTUATOR a biennial event bringing together leading experts, suppliers and users of new actuators and low-power electromagnetic drives. His research interests include medical device design, robotic co-manipulation and control of flexible instruments and robotic catheters.